Performance of activated stainless steel and nickel-based anodes in alkaline water electrolyser

Hamid R. Zamanizadeh [a,*], Alejandro. Oyarce Barnett [b,c], Svein Sunde [a], Bruno G. Pollet [b,d], Frode Seland [a]

[a] *Department of Materials Science and Engineering, Norwegian University of Science and Technology (NTNU), NO-7491, Trondheim, Norway*
[b] *Department of Energy and Process Engineering, Norwegian University of Science and Technology (NTNU), NO-7491, Trondheim, Norway*
[c] *Hystar AS, Veritasveien 5, 1363, Høvik, Norway*
[d] *Green Hydrogen Lab, Institute for Hydrogen Research (IHR), Université Du Québec à Trois-Rivières, 3351 Boulevard des Forges, Trois-Rivières, Québec, G9A 5H7, Canada*

HIGHLIGHTS

- SS316, SS304, Inconel718 and Incoloy800 are activated ex-situ toward OER.
- More Ni was obtained on SS316 and SS304 than on Inconel718 and Incoloy800.
- OER activity of the activated samples is linked to the surface Ni content.
- Short term and long term in-situ studies are performed on activated SS316.
- Successful activation of stainless steel 316 is obtained during in-situ operation.

ARTICLE INFO

ABSTRACT

Four different alloys including SS316, SS304, Inconel718 and Incoloy800 are activated by electro-oxidation at +1.70 V *vs.* RHE in 7.5 M KOH for 18 h. Their OER activity are evaluated *ex-situ* using linear sweep voltammetry in 1.0 M KOH in a three-electrode electrochemical cell. X-ray photoelectron microscopy and scanning electron microscopy are used to obtain the surface composition and surface morphology. It is found that the OER activity improves as the Ni content at the surface increases. A Ni mesh along with untreated and activated SS316 meshes were investigated *in-situ* in 30 wt% KOH at 80 °C in an alkaline electrolyser. The effect of temperature up to 80 °C as well as pressure up to 9 bar are studied on the cell performance. It is observed that the cell with activated SS316 as anode is outperforming those with the Ni and untreated SS316 as anode. Up to 255 h durability tests at constant current of 0.8 A cm^{-2} at 80 °C and 9 bar shows no degradation in the performance of the cells containing Ni and activated SS316 as anode. SS316 is also activated *in-situ* at 1.76 A cm^{-2} for 18 h and 2 bar. The *in-situ* activation improves the SS316 OER activity.

1. Introduction

Hydrogen produced by water electrolysis using renewable energy sources is an essential energy vector in the ongoing energy transition towards a zero-emission society. This so so-called green hydrogen can be utilized to help decarbonizing a wide range of high polluting sectors, e. g., ammonia production, glass industry, stainless steel production, as well as the transport sector, in particular heavy-duty transport applications. Making cost-effective green hydrogen is one of the main goal in the hydrogen value chain.

Water electrolysis is possible through alkaline water electrolysis (AWE), polymer electrolyte membrane water electrolysis (PEMWE) and solid oxide water electrolysis (SOWE). AWE is a reliable, safe, and mature industrial technology that uses non-noble catalysts and has relatively lower cost and longer lifetime [1–4]. The price of electrolytic hydrogen is directly related to the price of electricity and therefore improving the efficiency of electrolysers is one of the main drivers for further technology development. The hydrogen evolution reaction

* Corresponding author.
E-mail address: H.r.Zamanizadeh@gmail.com (H.R. Zamanizadeh).

(HER) and oxygen evolution reaction (OER) in water electrolysis are required to occur at a certain rate and as a result, significant activation overpotentials on the electrodes reduce electrolysis efficiency. Therefore, the development of cost-effective and active catalysts in the electrodes is a necessary mean towards the improvement of alkaline water electrolysis.

Among the non-noble metals, Ni and Ni containing compounds can provide significant properties as OER electrocatalysts [5]. Extensive research has been dedicated to the development of Ni-bimetallic compounds, among which, Ni–Fe has been found to provide lower OER overpotentials [6–11]. Therefore, Ni–Fe compounds with various ratios have been developed to optimize the activity [12–15]. However, there was no agreement on the optimum Ni to Fe ratio and a minimum of 10% and a maximum of 50% Fe seems to be the most effective. The effect of Fe is still being debated in the literature, among others, Friebel et al. [15] and Ahn et al. [16] showed that Fe is the active site in NiFeOOH phase.

State-of-the-art commercially available alkaline water electrolysers are composed of nickel as core and active material at both anode and cathode [17]. Ni–Fe-containing alloys, e.g., stainless steel, as cheaper alternatives to pure nickel have attracted attention recently as a possible OER electrode candidate. In good agreement with the works of Maurice et al. [18], several researchers have reported that Ni–Fe-containing alloys must undergo an electrochemical pretreatment in order to enrich the surface with Ni, and therefore to be reasonably active towards the OER [5,19–27]. For example, Moureaux et al. [24,25]. and Schäfer et al. [5] used electro-oxidation as a simple and promising method to enrich the surface with Ni. They reported improved catalytic activity attributed to a mixed metal oxide (MMO) formed on the surface. Researchers reported that substrate material, electrode potential, time and electrolyte in an electro-oxidation procedure affect the final surface composition [27–30] and hence expected to affect the OER catalytic activity.

In our previous work, we successfully activated SS316 by electro-oxidation in KOH electrolytes of various concentrations (1.0 M–12.5 M) and found that the surface composition can be tailored with pH [19]. The surface composition converged to 73% Ni and 27% Fe with increasing pH, also showing the highest OER performance of all activated samples [19].

Most research on electrodes for AWE have been performed using nanoparticle catalysts in a 3-electrode system such as a rotating disc electrode (RDE) or in a simplified test station employing mild conditions, e.g., lower electrolyte concentrations. However, it is imperative for the AWE industry to know how the electrodes perform under "real" conditions i.e., using concentrated KOH electrolytes (typically 30–40 wt %) at elevated pressures (e.g., 9 bar) and temperatures (e.g., 80 °C). Schalenbach et al. [31] evaluated polarization curve of a cell with thermally sprayed Raney-Ni (39 wt% Ni, 44 wt% Al and 17 wt% Mo) on perforated Ni electrodes at 80 °C and 1 bar. Colli et al. [32] presented the long term performance of a cell with Raney-Ni and untreated SS316 as cathode and anode, respectively, at 75 °C at 300 mA cm^2, with stable performance for the duration of 30 days.

In this work, we have employed an identical *ex-situ* activation procedure as in our previous work [19] on various Ni–Fe-containing materials (SS304, Inconel718 and Incoloy800) to investigate the resulting surface compositions and OER activity. *In-situ* measurements on untreated SS316, *ex-situ* activated SS316 and Ni-electrodes in a custom-made alkaline water electrolyser test station were performed to investigate whether *ex-situ* performance can be used as a reliable descriptor for true, *in-situ* performance. Furthermore, the effect of operating temperature (up to 80 °C) and pressure (up to 9 bar) on the overall cell performance was investigated. Long-term *in-situ* testing at 0.8 A cm^{-2} up to 255 h under "real" operating conditions was performed with Ni and *ex-situ* activated SS316 anodes. Post-mortem analyses after the long-term measurements were performed for both anode and cathode using SEM, XPS in addition to *ex-situ* electrochemical characterization. Finally, we investigated the feasibility of *in-situ* activation of

SS316 in a two-electrode cell in the alkaline test station.

2. Experimental

Ex-situ activation. Plate material that was cut into disc-shaped samples (∅ 5 mm), fixed with a conductive wire and molded in epoxy to be used as working electrode. Four different stainless-steel samples including SS316, SS304, Inconel718 and Incoloy800 are investigated in this study. The bulk compositions of the samples are given in Table 1. The samples were activated *ex-situ* in a conventional three-electrode electrochemical cell made of Teflon, used for the oxygen evolution reaction experiments. All *ex-situ* electrochemical measurements were carried out using a Gamry Reference 600™ potentiostat/galvanostat/ ZRA. For each pre-treatment, the working electrode (WE) (SS304, SS316, Inconel718 and Incoloy 800) was polished with 800, 1200 and 2200 SiC abrasive papers to a mirror finish and ultrasonically cleaned before electrochemical activation. A Hg/HgO, KOH (20%) (Koslow Scientific Company) and a silver (Ag) wire, which was wrapped around a PEEK rod, were used as reference electrode (RE) and counter electrode (CE), respectively. The samples were activated at a constant potential of +1.70 V *vs.* RHE in 7.5 M KOH solution for 18 h, see Ref. [19] for more information. The solutions were made by KOH pellets (Merck, >85%, product number: 105,033) and MiliQ water (18.2 M Ω). Two sets of *ex-situ* and *in-situ* electrochemical experiments were performed on the activated samples.

***Ex-situ* electrochemical investigation**. *Ex-situ* electrochemical investigations were carried out in a three-electrode electrochemical cell without cell separation in accordance with the specification mentioned in the previous paragraph. Linear sweep voltammograms (LSV, *I* vs. *E*) were generated from +1.48 V to +1.68 V *vs.* RHE at a potential scan rate of 5 mV min^{-1} (~0.0843 mV s^{-1}) and polarization curves (*E* vs. log(*j*)) were plotted to determine the OER activity of the different samples in 1.0 M KOH solution. LSV was repeated for activated 316 sample on three different samples to ensure the reproducibility of the results; for example, the current deviation measured at 1.55 V and 1.7 V were maximum 20% and 15%, respectively. LSVs in the HER region were recorded with a scan rate of 5 mV s^{-1} in 1.0 M KOH using a graphite rod as counter electrode.

Electrochemical surface area (ECSA) of the samples were estimated based upon measured capacitance. The capacitance values were extracted from CV measurements between +0.65 V and +0.75 V *vs.* RHE for scan rates of 20, 50, 100, 200 and 500 mV s^{-1}, and obtained as the slope of the plot of current (at +0.70 V *vs.* RHE) vs. scan rate [33]. It was assumed that no faradaic reactions occur in this potential region.

***In-situ* electrochemical investigation**: A single cell made of Ni parts with parallel flow field channels was used to perform *in-situ* analyses. Ni, SS316 and *ex-situ* activated SS316 mesh electrodes with 25 cm^2 geometric surface area and detailed specification mentioned in Fig. S1 from Strekkmetall AS were investigated as OER electrode. An electrode provided by Permascand AB was used as the cathode in all cell assemblies unless otherwise stated. The anode and cathode electrodes were placed on each side of a 500 μm thick Zirfon® composite membrane used as a separator. A pair of 0.25 mm thick Teflon gaskets were used to accommodate for the thickness of the electrode and optimize the contact forces between the separator, electrode and flow field. To ensure a proper sealing of the cell, both anode and cathode cell housing had an O-ring made of EPDM material. The cell was tightened up using 12 bolts by applying 20 N m torque on each bolt. Fig. S2 shows different steps in the cell assembly procedure.

The cell was then connected to a custom-built 800 W Greenlight E40 alkaline water electrolyser, which was filled with 30 wt% KOH (∼ 7.0 M KOH). The cell current was set to 5 A (0.2 A cm^{-2}) and the temperature was set to ramp from 25 °C to 80 °C corresponding to about 3 h. After the temperature stabilized at 80 °C, each cell was continuing to operate overnight (about 12 h) at a constant current of 5 A (0.2 A cm^{-2}) in 30 wt % KOH and 2 bar. This procedure was performed initially for all cells

Table 1
Compositions of various alloys used in this study reposted from supplier.

Alloy	Fe	Ni	Cr	Mn	Nb + Ta	Cu	Co	Mo	Other
SS316	61–72	10–14	16–18	2	–	–	–	2–3	Balance
SS 304	66–70	8–10.5	18–20	2	–	–	–	–	Balance
Incoloy 800	39.5	30–35	19–23	1.5	–	0.75	0.15–0.6	0.15–0.6	Balance
Inconel 718	22.5	50–55	17–21	0.35	4.75–5.5		1	2.8–3.3	Balance

and is referred to as "break-in procedure". Measurement of the conductivity of the electrolyte is a default feature of the test station and is measured simultaneously to all electrochemical tests.

The electrolyte was circulating with constant flow rate of 350–400 mL min^{-1} through the cell. Polarization curve and electrochemical impedance spectroscopy were recorded at different temperatures (50, 60, 70 and 80 °C) and pressures (2, 5, 7 and 9 bar). The polarization curve was obtained by applying small current steps within optimized time and were programmed to be stopped either at 2.1 V or 25 A (1 A cm^{-2}). The presented polarization curves are an average of forward and backward scans. Galvanostatic electrochemical impedance spectroscopy (EIS) was recorded from 100 kHz to 0.1 Hz with 5% perturbation of the applied current at 1.25 A, 2.5 A, 12.5 A and 18.75 A using a SP-150 BioLogic potentiostat coupled with a VMP3 booster. The data are shown from 9 kHz and lower for better visual representation of EIS data.

Durability tests were carried out using chronopotentiometry at constant current of 20 A (0.8 A cm^{-2}) at 80 °C and 9 bar for up to 255 h. Steady state polarization curves and galvanostatic EIS data were recorded within fixed time intervals during durability test. Small parts of the electrodes were cut for *post-mortem* analyses.

In-situ activation: SS316 as anode and Permascand electrode as cathode were activated *in-situ* by applying a cell current of 44 A (1.76 A cm^{-2}). This current was obtained from polarization curve of the *ex-situ* activated SS316 in 7.5 M KOH, corresponding to a potential of about +1.70 V *vs.* RHE on *ex-situ* activated SS316 and above +1.70 *vs.* RHE on *as*-received SS316. The current was applied for 18 h in the alkaline test rig employing 30 wt.% KOH at 25 °C and 2 bar. A standard break-in procedure was performed, and the cell was left to cool down to 25 °C prior to the described *in-situ* activation procedure. *In-situ* electrochemical tests after the *in-situ* activation was performed at 80 °C. Prior to this, a second break-in procedure (5 A current) was performed as part of the default procedure during reheating of the cell from 25 °C to 80 °C.

Surface characterization: Surface morphology was studied using high resolution FESEM (Zeiss Ultra 55) with a working voltage of 10 kV. Images were captured using a secondary electron detector. The FESEM was equipped with Energy Dispersive Spectroscopy (EDS) enabling us to do elemental analysis.

Surface composition was collected using Axis Ultra DLD XPS instrument (Kratos Analytical, Manchester, UK) with a monochromatic Al X-ray source. The X-ray source was emitted at a current of 10 mA and with an accelerating voltage of 10 kV. The binding energies were calibrated using C1s peak position (284.4 eV) as standard corresponding to adventitious carbon. The surface composition was calculated using a Shirley background and, Fe3p, Cr2p, Mn3p and Ni2p peaks in CasaXPS software.

3. Results and discussion

3.1. Ex-situ activation

Fig. 1 displays LSV curves (a) along with a figure showing the extracted potentials at 10 mA cm^{-2} and 2 mA cm^{-2} (b) for different samples in 1.0 M KOH. From the figure, it can be observed that all the activated samples are performing better than the non-activated samples, e.g., for the Incoloy800, the potential at 10 mA cm^{-2} decreased from +1.589 V to +1.554 V *vs.* RHE after activation. The potentials for activated samples at 10 mA cm^{-2} were determined to be +1.5295 V

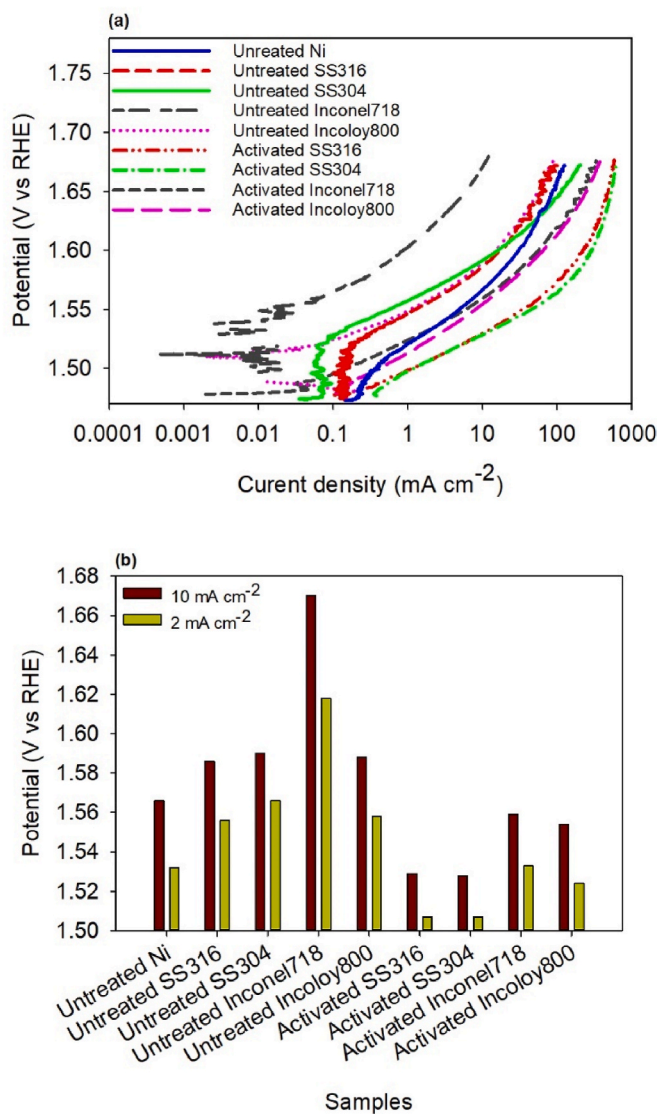**Fig. 1.** (a) *Ex-situ* polarization curves at 5 mV min^{-1} in 1.0 M KOH and room temperature and (b) Corresponding OER overpotential and onset potential extracted from (a) at 10 mA cm^{-2} and 2 mA cm^{-2}, respectively.

(SS316), +1.5282 V (SS304), +1.5590 V (Inconel718) and +1.5543 V (Incoloy800). Both the activated SS316 and SS304 exhibited more or less same performance and better than the activated Inconel718 and Incoloy800 samples.

The data in Fig. 1 are normalized with respect to the geometric surface area and an estimate of the electrochemical surface area (*ECSA*) is necessary to confirm the intrinsic performance of the activated samples. The measured double layer capacitances before and after activation are provided in Table 2 and shows indirectly the change in *ECSA* during activation. The maximum increase observed for all samples was found to be 25% for Incoloy800, which is lower than the increase in the catalytic activity. This suggests that the improvement in the performance is due to

Table 2

Double layer capacitances before and after activation.

Sample	C_{dl} (μF) (before activation)	C_{dl} (μF) (after activation)
SS316	12.70	10.7
Incoloy800	4.70	6.40
Inconel718	4.50	6.90
SS304	11.50	11.0

an increase in intrinsic catalytic activity rather than an increase in the surface area.

Table 3 shows XPS data on the surface of untreated and activated samples. The XPS data are measured on a range of samples and a root mean square deviation of the presented data in Table 3 are given in parentheses in front of each element. According to the data base presented by Shard et el. [34], the detection limit for Ni, Fe and Cr is smaller than 1 at.% when each of these elements are considered either as matrix or trace element. The surface composition on activated samples consists only of Ni and Fe. Here, both activated SS316 and activated SS304 have nearly 71–73% of Ni while activated Incoloy800 and Inconel718 contains lower Ni content, i.e., less than 47%. Even though the difference in bulk nickel composition of Incoloy800 and Inconel718 is significant (30–35 and 50–55 Ni, respectively) they both end up with about the same surface composition after activation, and significantly below the resulting Ni content for SS304 and SS316 samples. Ni and Fe were deconvoluted for activated SS316 as described in our previous work [19]. The increased Ni content on SS316 was previously explained in terms of the point defect model and was due to dissolution of Cr and Fe from the surface oxide into the electrolyte and subsequent enriching of the oxide with Ni [19]. A similar argument can be used for SS304, possessing a similar composition as SS316. The point-defect model of Macdonald [35] can also be used in an attempt to understand the lower increase in surface oxide Ni on high Ni-bulk materials. Ni is less readily oxidized than Cr and Fe [30] and it can be expected that the metal-oxide interface is more rapidly depleted by Cr and Fe as they are oxidized and transmitted to the oxide, leaving the metal side of the interface enriched with Ni metal. Due to the depletion of Cr and Fe, Ni at the metal-oxide interface will be more easily oxidized and transmitted to the oxide. In other words, the amount of Ni that will be oxidized and transmitted into the oxide depends upon the amount of Fe and Cr in the bulk metal. The higher the Ni content and the lower the Cr and Fe content in the metal, the less favourable oxidation and lower Ni content in the oxide. Alternatively, the amount of Fe that is possible to be incorporated into the Ni oxide can be expected to depend upon the amount of Ni in the bulk and therefore be different for the various materials used. Fe incorporated in the Ni-oxide is expected to be more stable [36]. These could be the reasons for the lower Fe content and higher Ni content in the surface oxides of SS316 and SS304 in comparison to Incoloy800 and Inconel700.

From these findings, we can conclude that the highest performance was obtained for the activated stainless steels with the lowest bulk Ni metal content. A low bulk Ni metal content yielded the highest Ni content in the surface oxide, which was previously also shown to depend upon the chemical environment [19].

Pure Ni has lower OER activity than other activated samples despite

its higher Ni due to promoting effect of Fe on the OER activity of Ni. Mixed metal oxide phases of Ni and Fe are proven to have synergistic effect towards the OER [13,14,37], where the optimum composition is enriched with Ni and depends upon the synthesis method. Qiu et al. [13] analyzed the OER activity of $Ni_yFe_{1-y}O_x$ amorphous nanoparticles supported on carbon in 1.0 M KOH and suggested that $Ni_{0.69}Fe_{0.31}O_x/C$ outperforming those with 17, 54 and 75 at. % Fe. The best composition reported by Qiu et al. [13] matches the composition on the activated SS316 and activated SS304 surfaces in this work. A Ni content higher than $\approx$ 73 at% Ni was not obtained on our samples with the activation procedure.

3.2. In-situ measurements

Fig. S3(a) shows *in-situ* single cell polarization curves at 2 bar and 50, 60, 70 and 80 °C, using an activated SS316 as the anode and a commercial electrode (Permascand) as the cathode. As the temperature rises the cell voltage decreases, e.g., the cell voltage at 0.75 A cm^{-2} drops from 2.06 V at 50 °C to 1.84 V at 80 °C and 2 bar. Galvanostatic EIS on the same cell (Fig. S3(b)) reveals that the cell resistance at 0.75 A cm^{-2} decreases from 407 mΩ cm^2 to 333 mΩ cm^2 as the temperature increases from 50 to 80 °C, respectively.

The activated SS316-Permascand cell is performing better, and the cell resistance is lower at higher temperatures. The reversible thermodynamic cell voltage at standard condition decreases with increasing temperature. This implies that the amount of electrical power required to split water, decreases with increasing the cell operating temperature [38]. Furthermore, a decrease in the cell resistivity is a result of improvement in separator conductivity and ion transport at higher temperatures. Therefore, increasing the cell temperature results in improving the cell performance due to improvement in electrolyte conductivity and reactions kinetics as well as lower thermodynamic cell voltage [38–40].

Fig. S4(a) represents polarization curves at various operating pressures, from 2 bar to 9 bar, at 80 °C on the activated SS316-Permascand cell. The cell performance is more or less the same at low current densities independent of the pressure, while the cell performs better at higher pressures when the current density is high, i.e., the cell voltage at 0.75 A cm^{-2} is 1.847 V at 2 bar and is higher than the cell voltage of 1.807 V at 9 bar. Galvanostatic EIS data on the same cell (Fig. S4(b)) reveals that the cell resistance at 0.75 A cm^{-2} decreases from 330 mΩ cm^2 to 262 mΩ cm^2 as the pressure increases from 2 to 9 bar, respectively.

According to the *Nernst equation*, an increase in the pressure leads to higher thermodynamic reversible cell voltage for water electrolysis [38, 41–43]. On the contrary, higher pressure would normally remove bubbles more efficiently from the electrodes and potentially reduce the shielding effect of bubbles that would cause higher cell resistance and mass transport constraints, i.e., at 0.75 A cm^{-2}. Consequently, the cell is performing better at higher pressures and at higher current densities as a result of faster gas removal and/or less shielding effects.

The same set of experiments with different temperatures and pressures were performed on the cells with either Ni or SS316 as anode. At high current densities the effect of pressure is larger on the cell with

Table 3

Surface oxide compositions from XPS measurements of the different alloys after and before activation.

Sample	Fe (at. %) ($\pm$4%)		Ni (at. %) ($\pm$4%)		Cr (at. %) ($\pm$0.5%)	
	Untreated	Activated	Untreated	Activated	Untreated	Activated
Incoloy800	>70.4	55.8	<10	44.2	19.6	0
Inconel718	> 59	53.2	<5	46.8	36	0
SS304	>77.5	29.1	<0.5	70.9	22	0
SS316	87	27.3	–	72.7	13	0
SS316 [25]	–	10	–	82.5	–	7.5
SS304 [21]	–	33	–	67	–	0

stainless-steel anodes than on the cell with Ni. This is probably originating from more effective gas bubble removal on the stainless-steel surface at high pressure (see Figs. S5 and S6). Based on this, the best condition for cell comparison is 80 °C and 9 bar, where the mass transport constraints and cell resistance are low. Consequently, all measurements from this point are carried out at these conditions.

Fig. 2(a) shows polarization curves at 80 °C and 9 bar for different cells with Ni, SS316 and activated SS316 as anode. Cell voltages at 0.75 A cm^{-2} were found to be 1.834 V, 1.914 V and 1.807 V for cells with Ni, SS316 and activated SS316, respectively, as anode. *iR* corrected cell voltages are extracted at four different current densities, 0.05, 0.1, 0.5 and 0.75 A cm^{-2}, and are shown in Fig. 2(b). The ranking as OER electrode is as follows: activated SS316 > Ni > SS316 when not *iR*-correcting and activated SS316 > SS316 > Ni when *iR*-correcting. Overall, activated SS316 is outperforming the Ni and SS316 with Ni being the poorest when *iR* losses are accounted for. The *iR* loss might have originated from the nature of the oxide on the surfaces, contact resistances, gas bubbles as well as resistances from the separator and the electrolyte.

It is worth pointing out that the *iR*-corrected polarization curves with SS316-Permascand cell are reproducible, well below the observed difference between the three anodes (see Fig. S7).

Ex-situ activated stainless steel outperforms nickel and untreated stainless steel, as expected from the *ex-situ* experiments. However,
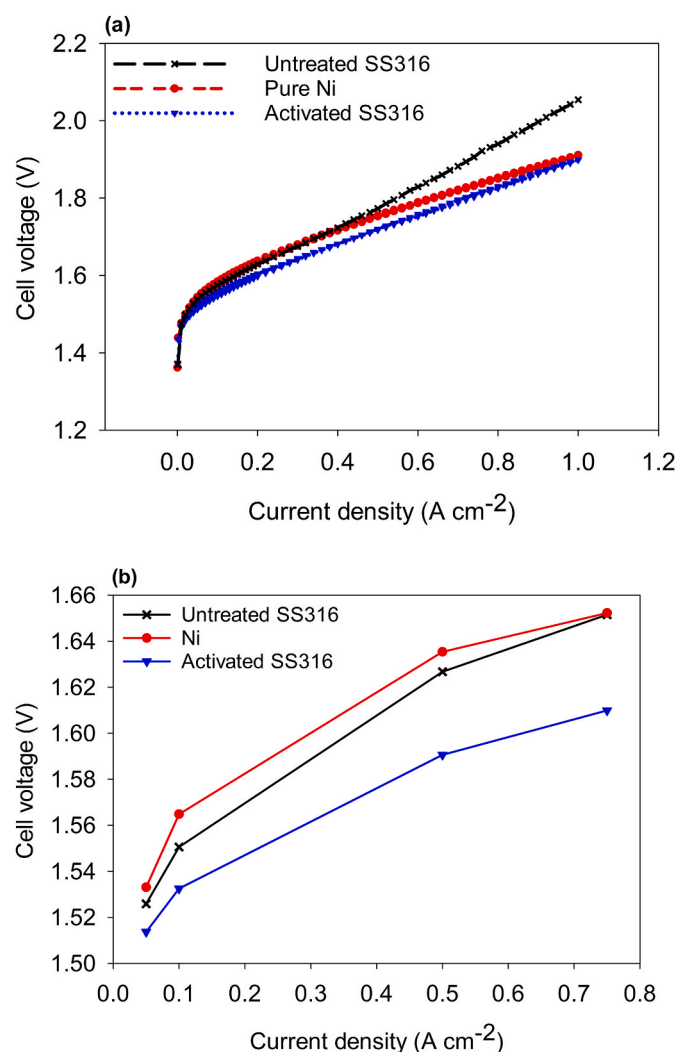
untreated SS316 performs better than pure Ni *in-situ* but not *ex-situ*. This can be explained by the surface composition and changes made during the break-in procedure. The surface of *as*-received polished SS316 is composed of 87% Fe and 13% Cr (Fig. S8(a)). However, XPS data confirms that the surface composition of this sample changed to 56% Ni, 40% Fe and 4% Cr after the break-in procedure (Fig. S8(b)). The break-in procedure involves applying a small oxidation current to the electrode in a high pH-environment, which we showed previously will increase the Ni content and reduce the Cr and Fe contents at the surface. This change will improve the OER activity of the SS316 sample and hence is the reason why the untreated sample performs better than the pure Ni sample, especially when comparing the *iR*-corrected cell performance. On the other hand, the *ex-situ* activated SS316 has nearly 73% Ni and 27% Fe on the surface, which improves the OER performance further, again in agreement with the *ex-situ* measurements.

The cell voltage in alkaline water electrolysis is largely affected by the cathode performance. This is illustrated in Fig. S9, which represents the effect of substituting a commercial Permascand cathode with a pure Ni cathode, obtaining a cell voltage of 1.64 V and 1.91 V at 0.20 A cm^{-2}, respectively.

Fig. S10 shows the galvanostatic EIS data at 0.1 A cm^{-2}, 80 °C and 9 bar for cells with SS316 or Ni as anode. The complex impedance plots show two suppressed semi-circles related to processes at the electrolyte-electrode interfaces. The EIS data are fitted to an equivalent circuit with two relaxations, LR$_1$(Q$_2$R$_2$) (Q$_3$R$_3$), (see inset of Fig. S10). The fitted data are summarised in Table 4. The high-frequency inductive behaviour is regarded as being due to experimental setup and is fitted with an inductor in series. The physical interpretation and meaning of this inductor are not considered further in this work. R$_1$ corresponds to all ohmic losses in the cell originating from the electrolyte, interfacial contact resistances, connections, and separator. The Ni-Permascand cell has a lower ohmic resistance, which is likely due to contact resistances. This was not investigated further.

Previously measured EIS data show that some of the *Nyquist plots* on electrolysers are composed of one depressed semi-circle [44,45], while others consist of two depressed semi-circles [46,47]. In acidic PEM systems, Dedigama et al. [44] suggested that only one charge transfer resistance belonging to the anode should be assigned in the equivalent circuit assuming that the cathode contribution can be neglected due to fast kinetics of the HER. On the other hand, in alkaline systems the HER is known to contribute significantly to the kinetic response of the system as seen in Fig. S9. Similarly, Faid et al. [47] indicated a large change in the resistance associated with one of the semi-circles upon changing the HER electrode from NiMo to Pt. As suggested by Sorsa et al. [48], there might also be other time constants but since their values are close to the other two time constants, their characteristics in the EIS data are combined. The parallel combinations of Q$_2$R$_2$ and Q$_3$R$_3$ must therefore account for all processes occurring at the electrode-electrolyte interfaces and are comprised of anode and cathode charge transfer resistances, adsorption of intermediates, mass transport resistances and effects of porous structures. The overall complexity associated with the system and the scattered data at low frequencies make it hard to directly assign the equivalent circuit parameters to system properties. Nevertheless, it is worth noting that the cell with activated SS316 as anode has the lowest R$_2$+R$_3$ value (i.e., *iR* compensated polarization resistance), which makes it a better candidate to be employed as anode in alkaline media.

3.3. Stability of the electrodes

Durability tests of Ni and activated SS316 as anodes are shown in Figs. 3 and 4, respectively. Fig. 3(a) shows the chronopotentiometry performance of the Ni-Permascand cell at constant current of 0.8 A cm^{-2} at 80 °C and 9 bar and Fig. 3(b) shows polarization curves measured at given times. Overall, the cell voltage increased slightly during the 223-h test; however, the polarization curves indicate a negligible change in the cell performance over time. Fig. S11 shows the iR corrected data that

Fig. 2. Steady state polarization curve for different anodes (a) not iR-corrected and (b) iR-corrected data at 80 °C and 9 bar.

Table 4
Elements in equivalent circuit model fitted to the Nyquist plot in Fig. S10.

Samples	L_1	R_1 (Ω cm^2)	R_2 (Ω cm^2)	Q_2 (F s^{a-1})	a_2	R_3 (Ω cm^2)	Q_3 (F s^{a-1})	a_3
Ni	5.3E-8	0.202	0.183	0.148	0.99	0.283	9.25	0.69
Untreated SS316	5.0E-8	0.253	0.168	0.31	1	0.273	11.64	0.72
Activated SS316	4E-8	0.254	0.15	0.756	1	0.232	11.1	0.8
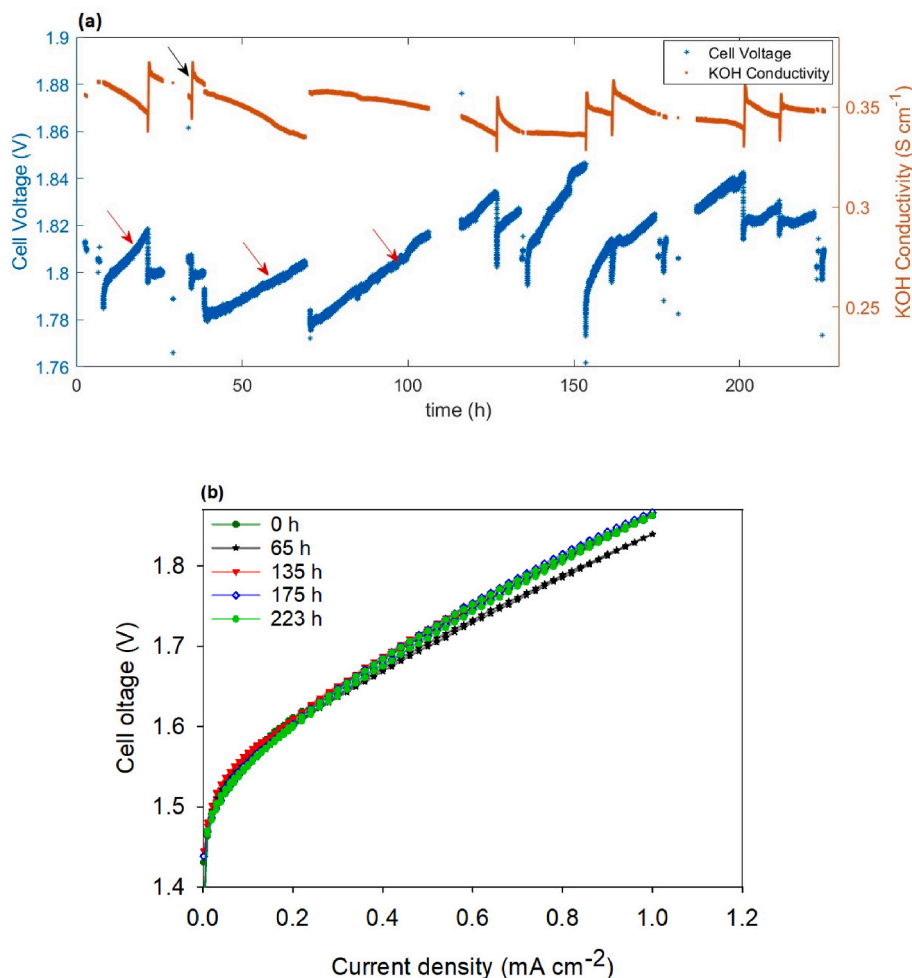
Fig. 3. (a) Chronopotentiometry at constant current of 0.8 A cm^{-2} at 80 °C and 9 bar for cell with Ni as anode, (b) steady state polarization curve recorded at different time intervals during the durability test, not-*iR* corrected.

confirm the negligible change after 223-h test. The cell voltage increased slightly within short time intervals (see e.g. sections indicated with the red arrows in Fig. 3(a)), which is correlated to a decrease in the KOH conductivity as shown in Fig. 3(a). The anode and cathode electrolyte compartment were set to segregated mode during operation, meaning that the KOH electrolyte of the anode and cathode loops are not continuously recombined yielding a drop in KOH conductivity and an increase in the cell voltage over time. Balancing of the KOH levels in the anode and cathode compartments was performed regularly, allowing for recombination of KOH (e.g. black arrow in Fig. 3(a)). These recombination processes are often accompanied with an increase in the KOH conductivity and a decrease in the cell voltage and is seen as sudden jumps in the long-term test. KOH recombination was also performed before each polarization measurement and after unplanned shutdowns. The breaks in long term durability correspond to either an emergency stop of the test station or a measurement of the polarization curve.

Fig. 4 shows the durability performance of the activated SS316-Permescand cell. The cell voltage decreased slightly over the 255-h

operation at a constant current of 0.8 A cm^{-2} at 80 °C and 9 bar. The polarization curves at selected times (Fig. 4(b)) show a similar improvement in the cell voltage. Here, we observe again that the cell voltage decreased after each KOH balancing, shutdown and before polarization measurement as a result of an increase in KOH conductivity and lower cell resistance. These data again confirm that the cell with activated stainless steel 316 is performing better than the cell with Ni.

The improvements seen in the polarization curves are not related to a change in the cell resistance itself because the cell resistance reverts to the same value after rebalancing, which is done prior to all polarization curves. This finding is in good agreement with the constant cell resistance extracted from the EIS measurements performed for each polarization curve. For example, a cell resistance of 0.2 Ω cm^2 was observed for all EIS at 0.1 A cm^{-2} at the given time intervals, see Fig. S12. Fig. S13 shows the *iR*-corrected data that confirm the overall cell performance improvement. The cell with activated SS316 is as stable as the cell with Ni and its performance even improves further with time.

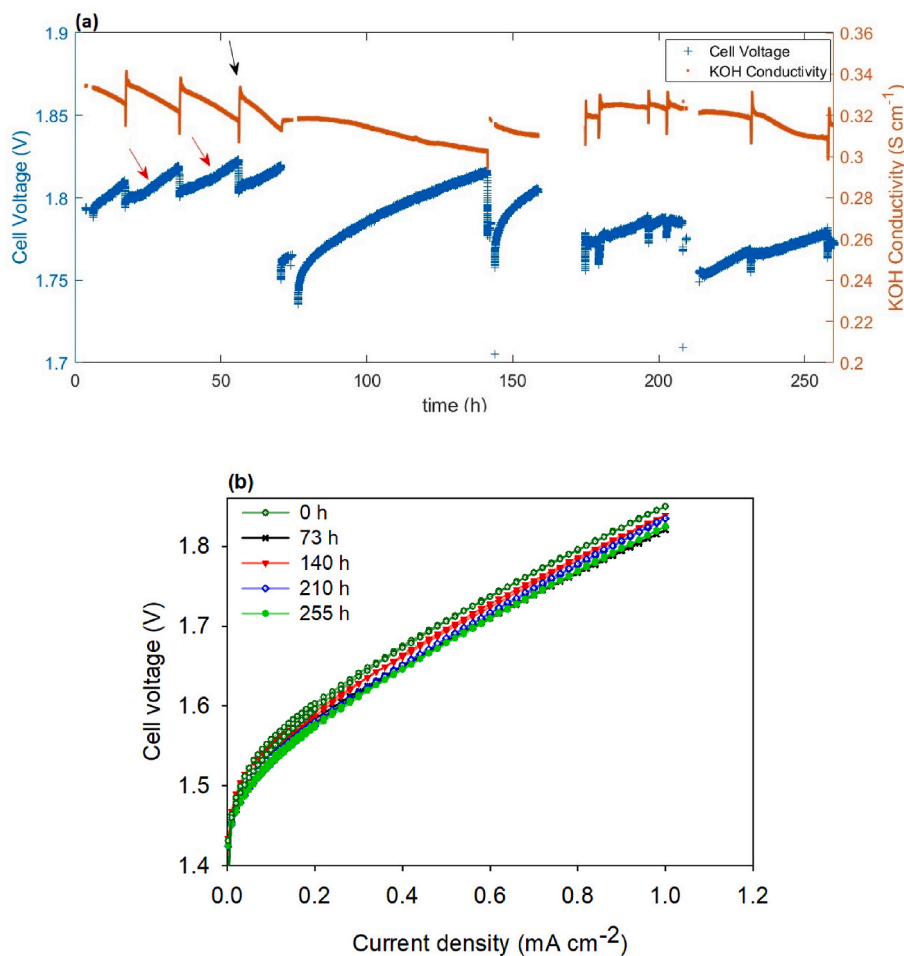Fig. 5 shows the *ex-situ* polarization curve of the activated SS316 in

Fig. 4. (a) Chronopotentiometry at constant current of 0.8 A cm^{-2} at 80 °C and 9 bar for cell with activated SS316 as anode, (b) steady state polarization curve recorded at different time intervals during the durability test, not-*IR* corrected.
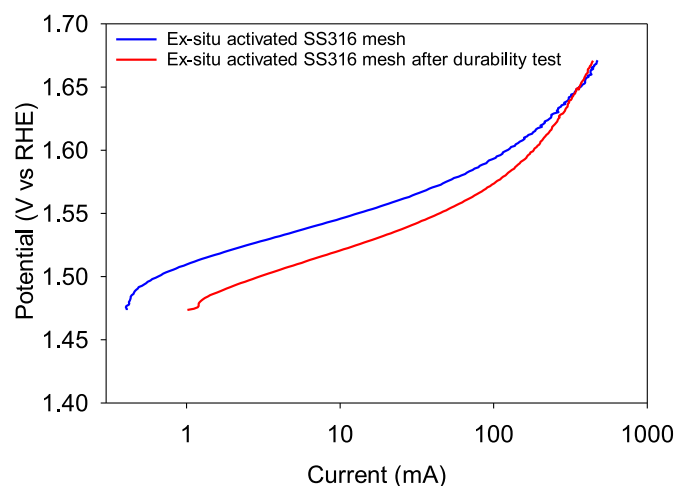

Fig. 5. *Ex-situ* polarization curves of ex-situ activated SS316 in 1 M KOH before and after 255 h at constant current of 0.8 A cm^{-2}, 80 °C and 9 bar in 30 wt % KOH.

1.0 M KOH before and after the durability test. There is a noticeable decrease in electrode potential for the electrode before and after the 255-h *in-situ* durability test, decreasing from 1.546 V to 1.520 V at 10 mA, respectively. These data indicate that the performance of activated SS316 as anode was improved further over time during the durability

test.

Fig. 6 shows the SEM images of the activated SS316 (a) before and (b) after the 255-h durability test in 30 wt% KOH at 0.8 A cm^{-2}, 80 °C and 9 bar. It is obvious that the morphology of the anode changed during the durability test, with a much more roughened electrode surface after the test (Fig. 6(b)). Such a roughening is most likely to be due to a dissolution and redeposition process from dissolved metal ions due to the lowering of the local pH at the surface during OER. A lower pH at the surface will shift the equilibria from ions in the electrolyte to deposition of hydroxides on the surface (see e.g., Ni stability in electrolyte in Ref. [49]). This will also occur on inherently stable electrodes during OER if the electrolyte contains dissolved metal ions that can deposit if the pH is lowered. A similar morphology (Fig. 6(b)) was also observed by Shihui Zou et al. [50], when they electrodeposited Fe(oxy)hydroxide on Au or Pt cathodes.

XPS data of the activated SS316 surface before (Table 2) and after the durability test (Fig. S14) show a decrease in the Ni content from 72.7% to 38.5% and an increase in the Fe and Cr contents from 27.3 to 49.5% and 0–12%, respectively. Considering our previous findings, a lower Ni content would yield a lower OER performance, however, this can be expected to be somewhat compensated due to the presence of Cr on the surface [19]. Furthermore, the observed increased coarsening would yield a higher surface area and hence higher OER currents. This could explain the improved performance after the durability test, despite the less optimum surface composition. At higher current densities, the performance is declining in comparison to the activated sample before durability test (Fig. 5). We may assign this observation to the trapping of
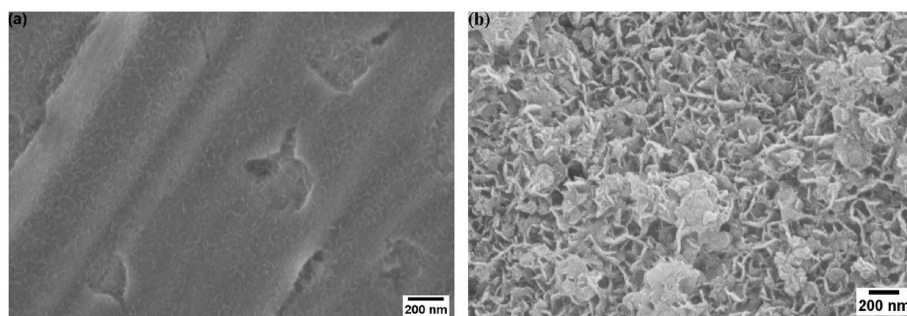
Fig. 6. SEM morphology image of *ex-situ* activated SS316 (a) before and (b) after 255 h at constant current of 0.8 A cm^{-2}, 80 °C and 9 bar in 30 wt% KOH.

gas bubbles in the porous structure, lowering the available surface area.

Fig. 7 shows the *ex-situ* polarization curves of the Permascand electrode, which was used as cathode within the same cell, before and after durability test. The HER activity of the Permascand electrode was significantly improved after the 255-h durability test. Again, this can be explained in terms of an increased surface area, which is seen from the SEM images in Fig. 8, showing the Permascand cathode (a) before and (b) after the durability test. EDS analysis of the electrode indicates that the surface composition changed significantly during the long-term in-situ measurement due to deposition of Cu, Cr and Fe impurities from the electrolyte (Fig. S15). Finally, both the anode and cathode performance increased after the 255-h durability test due to the increased surface areas, which resulted in an overall improved cell performance.

3.4. In-situ activation

As seen earlier, the break-in procedure improved the cell performance noticeably by changing the surface composition of the *as-received* SS316 anode. However, the break-in procedure involves a much lower current density (0.20 A cm^{-2} geometric) than the current density necessary to achieve the most active surface composition of SS316. This was discussed in more detail in our previous work where an activation potential of about +1.70 V *vs.* RHE was required to yield a surface of 73% Ni and 27% Fe in 7.5 M KOH [19]. Here, we are assessing the possibility of omitting such an *ex-situ* activation step by activating the anode *in-situ*, hence applying a geometric current density of 1.80 A cm^{-2} (equivalent to potential of higher than +1.70 V *vs.* RHE on the *as-received* SS316) for 18 h as part of a modified break-in and activation procedure.
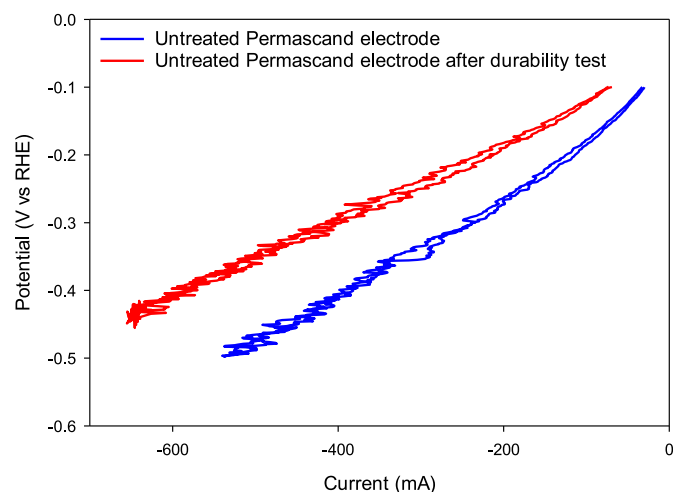

Fig. 7. Polarization curve in 1.0 M KOH with a scan rate of 5 mV s^{-1} using a before and after 255 h *in-situ* operation at 0.8 A cm^{-2}, 80 ° C and 9 bar in 30 wt % KOH.

Fig. S16 shows polarization curves of a SS316 anode - Permascand cathode cell before and after *in-situ* activation. The milder break-in procedure was carried out prior to the polarization curve in both cases. The overall cell performance is almost the same before and after the *in-situ* activation procedure and an increased current density does not seem to provide a more active anode.

Ex-situ polarization curves of SS316 mesh anodes *as-received* and after *in-situ* activation, and Permascand cathode show a significant increase in the performance towards both the OER and the HER, respectively, after *in-situ* activation (see Fig. S17 (a) and (b)). However, it is not straightforward to relate the individual electrode improvements to the performance of the SS316-Permascand cell after the break-in procedure and after the *in-situ* activation.

Fig. S18 shows a SEM image of SS316 after *in-situ* activation, with small surface features appearing after the activation. These surface features are similar to those observed after *ex-situ* activation (Fig. 6(a)). XPS data of the SS316 anode after the *in-situ* activation revealed that the surface composition was 55.20% Ni, 27.20% Fe, 2% Cr and 15.60% Mn (Fig. S19). The amount of Ni obtained after *in-situ* activation is the same as amount of Ni after break-in procedure and the only difference observed is the presence of Mn in the surface oxide after *in-situ* activation. Mn was not observed in the surface oxide after *ex-situ* activation (Table 2). The *in-situ* activation was current controlled and a higher anode potential than +1.70 V *vs.* RHE (higher than the potential used for the break-in procedure and *ex-situ* activation) might lead to the presence of Mn in the surface oxide. On the other hand, a very low (negative) cathode potential could lead to the deposition of metal impurities at the cathode.

Fig. S20 shows a SEM image of the Permascand electrode after the *in-situ* activation. It was concluded from EDS analyses that a significant deposition of metal impurities, primarily consisting of Fe, Cr and Cu, occurred. The uneven, dendritic structure suggests that the deposition is diffusion limited and depends upon the concentration of metal ions in the electrolyte.

Overall, both the anode and cathode electrodes performance improved after *in-situ* activation compared to the *as-received* electrodes due to more optimized surface compositions and/or roughening of the electrodes, yielding an increase in the surface area. However, the improvement or deterioration of the anode and cathode performances after the break-in procedure and after *in-situ* activation, nullifying each other, led to a same overall cell performance.

4. Conclusions

The OER activity of Ni containing alloys is dependent upon the surface composition. Surface compositions of Incoloy800, Inconel718, SS316 and SS304 can be altered *ex-situ* electrochemically at a constant potential of +1.70 V *vs.* RHE in 7.5 M KOH for 18 h. In this way, it is possible to activate the electrode and achieve a better OER activity. XPS revealed that none of the *ex-situ* activated samples contained Cr on the surface. Better OER activities were related to the enrichment of Ni on the
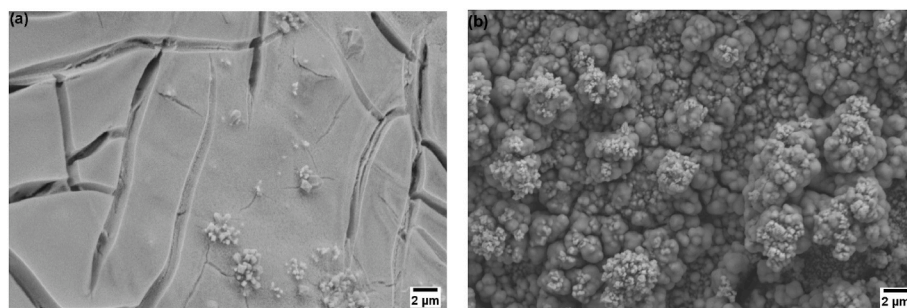
Fig. 8. SEM images of the Permascand cathode morphology (a) before and (b) after 255 h of *in-situ* operation at 0.8 A cm^{-2}, 80 $^\circ$C and 9 bar in 30 wt% KOH.

activated surfaces. Activated SS316 and activated SS304 had a higher amount of Ni, i.e., around 73% Ni, and lower OER overpotential compared to the activated Incoloy800 and activated Inconel718 with around 45% Ni. *In-situ* analyses in a two-electrode cell revealed that activated SS316 as anode outperformed the Ni or *as*-received SS316, for example, the cell voltage of 1.826 V was obtained at 0.8 A cm^{-2} for the cell with activated SS316 as anode compared to a cell voltage of 1.852 V for the cell with Ni as anode. Durability measurements showed that the activated SS316 performance improved over 255 h at 80 $^\circ$C and 9 bar. This improvement was attributed to an increased surface area of both anode and cathode.

An *in-situ* activation procedure was effective to activate the *as*-received SS316 for OER.

CRediT authorship contribution statement

Hamid R. Zamanizadeh: Conceptualization, Data curation, Formal analysis, Investigation, Methodology, Visualization, Writing – original draft, Writing – review & editing. **Alejandro. Oyarce Barnett:** Data curation, Investigation, Writing – review & editing, Validation. **Svein Sunde:** Supervision, Conceptualization, Writing – review & editing, Validation. **Bruno G. Pollet:** Supervision, Conceptualization, Writing – review & editing, Validation. **Frode Seland:** Supervision, Project administration, Conceptualization, Validation, Resources, Writing – review & editing, Funding acquisition.

Declaration of competing interest

The authors declare that they have no known competing financial interests or personal relationships that could have appeared to influence the work reported in this paper.

Data availability

Data will be made available on request.

Acknowledgement

Appendix A. Supplementary data

Supplementary data to this article can be found online at https://doi.org/10.1016/j.jpowsour.2023.232828.

References

[1] M. David, C. Ocampo-Martínez, R. Sánchez-Peña, Advances in alkaline water electrolyzers: a review, J. Energy Storage 23 (2019) 392–403.

[2] A. Ursua, L.M. Gandia, P. Sanchis, Hydrogen production from water electrolysis: current status and future trends, Proc. IEEE 100 (2) (2011) 410–426.

[3] S. Marini, P. Salvi, P. Nelli, R. Pesenti, M. Villa, M. Berrettoni, G. Zangari, Y. Kiros, Advanced alkaline water electrolysis, Electrochim. Acta 82 (2012) 384–391.

[4] A. Buttler, H. Spliethoff, Current status of water electrolysis for energy storage, grid balancing and sector coupling via power-to-gas and power-to-liquids: a review, Renew. Sustain. Energy Rev. 82 (2018) 2440–2454.

[5] H. Schäfer, D.M. Chevrier, P. Zhang, J. Stangl, K. Müller-Buschbaum, J.D. Hardege, K. Kuepper, J. Wollschläger, U. Krupp, S. Dühnen, Electro-oxidation of Ni42 steel: a highly active bifunctional electrocatalyst, Adv. Funct. Mater. 26 (35) (2016) 6402–6417.

[6] X. Li, F.C. Walsh, D. Pletcher, Nickel based electrocatalysts for oxygen evolution in high current density, alkaline water electrolysers, Phys. Chem. Chem. Phys. 13 (3) (2011) 1162–1167.

[7] L. Trotochaud, J.K. Ranney, K.N. Williams, S.W. Boettcher, Solution-cast metal oxide thin film electrocatalysts for oxygen evolution, J. Am. Chem. Soc. 134 (41) (2012) 17253–17261.

[8] M.D. Merrill, R.C. Dougherty, Metal oxide catalysts for the evolution of O2 from H2O, J. Phys. Chem. C 112 (10) (2008) 3655–3666.

[9] M.S. Burke, L.J. Enman, A.S. Batchellor, S. Zou, S.W. Boettcher, Oxygen evolution reaction electrocatalysis on transition metal oxides and (oxy) hydroxides: activity trends and design principles, Chem. Mater. 27 (22) (2015) 7549–7558.

[10] D.A. Corrigan, R.M. Bendert, Effect of coprecipitated metal ions on the electrochemistry of nickel hydroxide thin films: cyclic voltammetry in 1M KOH, J. Electrochem. Soc. 136 (3) (1989) 723–728.

[11] R.L. Tichenor, Nickel oxides-relation between electrochemical and foreign ion content, Ind. Eng. Chem. 44 (5) (1952) 973–977.

[12] D.A. Corrigan, The catalysis of the oxygen evolution reaction by iron impurities in thin film nickel oxide electrodes, J. Electrochem. Soc. 134 (2) (1987) 377–384.

[13] Y. Qiu, L. Xin, W. Li, Electrocatalytic oxygen evolution over supported small amorphous Ni–Fe nanoparticles in alkaline electrolyte, Langmuir 30 (26) (2014) 7893–7901.

[14] J. Landon, E. Demeter, N. Inoglu, C. Keturakis, I.E. Wachs, R. Vasic, A.I. Frenkel, J. R. Kitchin, Spectroscopic characterization of mixed Fe–Ni oxide electrocatalysts for the oxygen evolution reaction in alkaline electrolytes, ACS Catal. 2 (8) (2012) 1793–1801.

[15] D. Friebel, M.W. Louie, M. Bajdich, K.E. Sanwald, Y. Cai, A.M. Wise, M.-J. Cheng, D. Sokaras, T.-C. Weng, R. Alonso-Mori, Identification of highly active Fe sites in (Ni, Fe) OOH for electrocatalytic water splitting, J. Am. Chem. Soc. 137 (3) (2015) 1305–1313.

[16] H.S. Ahn, A.J. Bard, Surface interrogation scanning electrochemical microscopy of Ni1−x Fe x OOH (0< x< 0.27) oxygen evolving catalyst: kinetics of the "fast" iron sites, J. Am. Chem. Soc. 138 (1) (2016) 313–318.

[17] M. Schalenbach, A.R. Zeradjanin, O. Kasian, S. Cherevko, K.J. Mayrhofer, A perspective on low-temperature water electrolysis–challenges in alkaline and acidic technology, Int. J. Electrochem. Sci. 13 (2) (2018) 1173–1226.

[18] V. Maurice, W. Yang, P. Marcus, X-Ray photoelectron spectroscopy and scanning tunneling microscopy study of passive films formed on (100) Fe-18Cr-13Ni single-crystal surfaces, J. Electrochem. Soc. 145 (3) (1998) 909.

[19] H.R. Zamanizadeh, S. Sunde, B.G. Pollet, F. Seland, Tailoring the oxide surface composition of stainless steel for improved OER performance in alkaline water electrolysis, Electrochim. Acta (2022) 140561.

[20] H. Schäfer, S.M. Beladi-Mousavi, L. Walder, J. Wollschläger, O. Kuschel, S. Ichilmann, S. Sadaf, M. Steinhart, K. Küpper, L. Schneider, Surface oxidation of stainless steel: oxygen evolution electrocatalysts with high catalytic activity, ACS Catal. 5 (4) (2015) 2671–2680.

[21] H. Schäfer, S. Sadaf, L. Walder, K. Kuepper, S. Dinklage, J. Wollschläger, L. Schneider, M. Steinhart, J. Hardege, D. Daum, Stainless steel made to rust: a robust water-splitting catalyst with benchmark characteristics, Energy Environ. Sci. 8 (9) (2015) 2685–2697.

[22] S. Anantharaj, M. Venkatesh, A.S. Salunke, T.V. Simha, V. Prabu, S. Kundu, High-performance oxygen evolution anode from stainless steel via controlled surface oxidation and Cr removal, ACS Sustain. Chem. Eng. 5 (11) (2017) 10072–10083.

[23] H. Zhong, J. Wang, F. Meng, X. Zhang, In situ activating ubiquitous rust towards low-cost, efficient, free-standing, and recoverable oxygen evolution electrodes, Angew. Chem. Int. Ed. 55 (34) (2016) 9937–9941.

[24] F. Moureaux, P. Stevens, G. Toussaint, M. Chatenet, Development of an oxygen-evolution electrode from 316L stainless steel: application to the oxygen evolution reaction in aqueous lithium–air batteries, J. Power Sources 229 (2013) 123–132.

[25] F. Moureaux, P. Stevens, G. Toussaint, M. Chatenet, Timely-activated 316L stainless steel: a low cost, durable and active electrode for oxygen evolution reaction in concentrated alkaline environments, Appl. Catal. B Environ. 258 (2019), 117963.

[26] S.N. Sampathkumar, T.B. Ferriday, P.H. Middleton, J. Van Herle, Activation of stainless steel 316L anode for anion exchange membrane water electrolysis, Electrochem. Commun. 146 (2023), 107418.

[27] M. Chatenet, B.G. Pollet, D.R. Dekel, F. Dionigi, J. Deseure, P. Millet, R.D. Braatz, M.Z. Bazant, M. Eikerling, I. Staffell, Water Electrolysis: from Textbook Knowledge to the Latest Scientific Strategies and Industrial Developments, Chemical Society Reviews, 2022.

[28] I. Hamidah, A. Solehudin, A. Setiawan, A. Hamdani, M.A.S. Hidayat, F. Adityawarman, F. Khoirunnisa, A.B.D. Nandiyanto, Corrosion study of AISI 304 on KOH, NaOH, and NaCl solution as an electrode on electrolysis process, J. Eng. Sci. Technol. 13 (5) (2018) 1345–1351.

[29] L. Freire, M.A. Catarino, M. Godinho, M. Ferreira, M. Ferreira, A. Simões, M. Montemor, Electrochemical and analytical investigation of passive films formed on stainless steels in alkaline media, Cement Concr. Compos. 34 (9) (2012) 1075–1081.

[30] C.-O. Olsson, D. Landolt, Passive films on stainless steels—chemistry, structure and growth, Electrochim. Acta 48 (9) (2003) 1093–1104.

[31] M. Schalenbach, G. Tjarks, M. Carmo, W. Lueke, M. Mueller, D. Stolten, Acidic or alkaline? Towards a new perspective on the efficiency of water electrolysis, J. Electrochem. Soc. 163 (11) (2016) F3197.

[32] A.N. Colli, H.H. Girault, A. Battistel, Non-precious electrodes for practical alkaline water electrolysis, Materials 12 (8) (2019) 1336.

[33] M. Kölbach, S. Fiechter, R. van de Krol, P. Bogdanoff, Evaluation of electrodeposited α-Mn2O3 as a catalyst for the oxygen evolution reaction, Catal. Today 290 (2017) 2–9.

[34] A.G. Shard, Detection limits in XPS for more than 6000 binary systems using Al and Mg Kα X-rays, Surf. Interface Anal. 46 (3) (2014) 175–185.

[35] D.D. Macdonald, The history of the point defect model for the passive state: a brief review of film growth aspects, Electrochim. Acta 56 (4) (2011) 1761–1772.

[36] M.S. Burke, M.G. Kast, L. Trotochaud, A.M. Smith, S.W. Boettcher, Cobalt–iron (oxy) hydroxide oxygen evolution electrocatalysts: the role of structure and composition on activity, stability, and mechanism, J. Am. Chem. Soc. 137 (10) (2015) 3638–3648.

[37] Z. Zhao, H. Wu, H. He, X. Xu, Y. Jin, Self-standing non-noble metal (Ni–Fe) oxide nanotube array anode catalysts with synergistic reactivity for high-performance water oxidation, J. Mater. Chem. 3 (13) (2015) 7179–7186.

[38] P. Millet, S. Grigoriev, Water Electrolysis Technologies, Renewable Hydrogen Technologies: Production, Purification, Storage, Applications and Safety, 2013, pp. 19–41.

[39] M. Miles, G. Kissel, P. Lu, S. Srinivasan, Effect of temperature on electrode kinetic parameters for hydrogen and oxygen evolution reactions on nickel electrodes in alkaline solutions, J. Electrochem. Soc. 123 (3) (1976) 332.

[40] J.C. Ganley, High temperature and pressure alkaline electrolysis, Int. J. Hydrogen Energy 34 (9) (2009) 3604–3611.

[41] M. Shen, N. Bennett, Y. Ding, K. Scott, A concise model for evaluating water electrolysis, Int. J. Hydrogen Energy 36 (22) (2011) 14335–14341.

[42] J. Larminie, A. Dicks, M.S. McDonald, Fuel Cell Systems Explained, J. Wiley, Chichester, UK, 2003.

[43] D. Todd, M. Schwager, W. Mérida, Thermodynamics of high-temperature, high-pressure water electrolysis, J. Power Sources 269 (2014) 424–429.

[44] I. Dedigama, P. Angeli, K. Ayers, J. Robinson, P. Shearing, D. Tsaoulidis, D. Brett, In situ diagnostic techniques for characterisation of polymer electrolyte membrane water electrolysers–Flow visualisation and electrochemical impedance spectroscopy, Int. J. Hydrogen Energy 39 (9) (2014) 4468–4482.

[45] E. Cossar, A. Oyarce Barnett, F. Seland, E.A. Baranova, The performance of nickel and nickel-iron catalysts evaluated as anodes in anion exchange membrane water electrolysis, Catalysts 9 (10) (2019) 814.

[46] S. Sun, Z. Shao, H. Yu, G. Li, B. Yi, Investigations on degradation of the long-term proton exchange membrane water electrolysis stack, J. Power Sources 267 (2014) 515–520.

[47] A.Y. Faid, A. Oyarce Barnett, F. Seland, S. Sunde, Highly active nickel-based catalyst for hydrogen evolution in anion exchange membrane electrolysis, Catalysts 8 (12) (2018) 614.

[48] O. Sorsa, J. Nieminen, P. Kauranen, T. Kallio, Stable reference electrode in polymer electrolyte membrane electrolyser for three-electrode measurements, J. Electrochem. Soc. 166 (16) (2019) F1326.

[49] S. Yang, J. Li, D. Shao, J. Hu, X. Wang, Adsorption of Ni (II) on oxidized multi-walled carbon nanotubes: effect of contact time, pH, foreign ions and PAA, J. Hazard Mater. 166 (1) (2009) 109–116.

[50] S. Zou, M.S. Burke, M.G. Kast, J. Fan, N. Danilovic, S.W. Boettcher, Fe (oxy) hydroxide oxygen evolution reaction electrocatalysis: intrinsic activity and the roles of electrical conductivity, substrate, and dissolution, Chem. Mater. 27 (23) (2015) 8011–8020.